PHYSICAL REVIEW D **106,** 094502 (2022)

Toward the real-time evolution of gauge-invariant $\mathbb{Z}_2$ and $U(1)$ quantum link models on noisy intermediate-scale quantum hardware with error mitigation

Emilie Huffman,[1] Miguel García Vera,[2] and Debasish Banerjee[3,4]
[1]Perimeter Institute For Theoretical Physics, Waterloo, Ontario N2H6T7, Canada
[2]Departamento de Física, Escuela Politécnica Nacional,
Avenida Ladrón de Guevara E11-253, Quito, Ecuador
[3]Saha Institute of Nuclear Physics, HBNI, 1/AF Bidhannagar, Kolkata 700064, India
[4]Homi Bhabha National Institute, Training School Complex, Anushaktinagar, Mumbai 400094, India

(Received 21 December 2021; revised 9 July 2022; accepted 21 September 2022; published 10 November 2022)

Practical quantum computing holds clear promise in addressing problems not generally tractable with classical simulation techniques, and some key physically interesting applications are those of real-time dynamics in strongly coupled lattice gauge theories. In this article, we benchmark the real-time dynamics of $\mathbb{Z}_2$ and $U(1)$ gauge-invariant plaquette models using noisy intermediate-scale quantum (NISQ) hardware, specifically the superconducting-qubit-based quantum IBM Q computers. We design quantum circuits for models of increasing complexity and measure physical observables such as the return probability to the initial state and locally conserved charges. NISQ hardware suffers from significant decoherence and a corresponding difficulty to interpret the results. We demonstrate the use of hardware-agnostic error mitigation techniques, such as circuit folding methods implemented via the *Mitiq* package, and we show what they can achieve within the quantum volume restrictions for the hardware. Our study provides insight into the choice of Hamiltonians, the construction of circuits, and the utility of error mitigation methods to devise large-scale quantum computation strategies for lattice gauge theories.

DOI: 10.1103/PhysRevD.106.094502

I. INTRODUCTION

Gauge theories are a cornerstone in the description of various naturally occurring phenomena in nature, whether in particle or in condensed matter physics [1]. These theories are characterized by the presence of local conservation laws, which are in general not enough to make the models integrable. However, such local conservation laws greatly constrain these systems, leading to exotic phenomena involving quantum entanglement of the fundamental degrees of freedom over long distances, many of which remain unexplored due to computational difficulties with studying them on a classical computer. In addition, one of the outstanding challenges in fundamental physics is to study the real-time dynamics of the quantum entanglement inherent in gauge theories that leads to confinement. The rapid experimental development of quantum computers (both analog and digital) [2–6] following the pioneering suggestion of Feynman [7] provides an opportunity to overcome these bottlenecks and make new fundamental progress in this field.

While certain initial exciting developments have been obtained from the studies of finite, relatively small systems using classical computations such as exact diagonalization and variational methods using the MPS *Ansätze*, it is pertinent to understand the corresponding behavior in large quantum systems. This is an exponentially difficult problem in the system size for most of the classical computational methods in use, thus demanding the use of new toolboxes such as quantum computers. Although theoretically promising, current quantum computers in use are either of the analog variety, where a certain experimental setup can very efficiently emulate only a limited variety of physical systems, or of the digital kind, which are limited by the moderate number of available (noisy) qubits. There has, however, been some progress toward the development of hybrid analog-digital approaches with the aim to combine the desirable features of both [8]. For the case of digital quantum computation, which will be our main focus in this article, it becomes important to devise efficient optimizations of the quantum circuitry so that the studies can be extended to large quantum systems. The results need to be benchmarked from an independent computational method at small or medium system sizes. While such studies have been extensively carried out for spin models, implementations of quantum link models on quantum hardware are relatively scarce, a gap which our article aims to fill.

Moreover, one of the crucial theoretical physics problems where quantum computers could play a central role is establishing the emergence of thermalization in isolated many-body quantum systems, necessary to describe equilibrium properties of the system using quantum statistical mechanics [9,10]. This has become well known in the literature under the eigenstate thermalization hypothesis (ETH). On the other hand, in the absence of thermalization, the properties of the initial states are preserved for a long time, and the growth of quantum entanglement is very slow. This is known to occur in the many-body localized (MBL) phases [11] and has raised the possibility of using such phases as quantum memories, which can encode quantum information with high fidelity [12]. Confining phases of gauge theories could potentially offer the possibility of realizing topologically stable qubits, unaffected by local decoherent noise, and act as quantum memories. Another relatively new development is the discovery of atypical quantum states in (strongly) interacting quantum systems, dubbed as quantum many-body scars [13], which do not follow the ETH, unlike other quantum states. Even though such states belong to the highly excited part of the energy spectrum, they have anomalously low entropy. Studying properties of such quantum states on large systems would also benefit from a quantum computer, given the computational complexity for classical simulation methods.

In the context of particle physics, especially for nonperturbative *ab initio* computations in lattice chromodynamics (LQCD), a plethora of questions involving physics at real time and high baryon density cannot be reliably answered using classical algorithms running on classical computers. Quantum computers, both analog and digital, have been proposed in order to make progress on this front [14]. Several pioneering experiments [15–20] have already demonstrated the possibility of harnessing the new technology to address questions posed in the context of high-energy physics (HEP). Further, the availability of noisy intermediate-scale (universal) quantum computers from the IBM and the Rigetti corporations have empowered the theorists to perform experiments. Recently, there have been many such preliminary efforts to address representative questions in simpler gauge theories using quantum computing techniques. These include the investigation of scattering and real-time dynamics in spin systems [21–23] and in gauge theories [24,25], and static charges in gauge theories [26], as well as mass spectra in Abelian and non-Abelian lattice gauge theories [27,28]. Naturally, the efforts to represent only physical states of the corresponding gauge theory Hamiltonian, which are invariant under the Gauss law, in the limited quantum hardware available to us have spurred a cascade of theoretical developments [29–40].

A major obstacle in the design of quantum circuits and quantum algorithms is the decoherence of the superconducting qubits in contemporary quantum computers, also called noisy intermediate-scale quantum (NISQ) devices, such as the IBM Q and the Rigetti platforms. The qubits in these devices are only approximately isolated from the environment, and the gate operations needed to induce some interaction terms among them also depend on whether the operation is a single, or a multiqubit operation (the latter have smaller fidelities). Moreover, single-gate operations can have different gate times depending on the specific qubit they are applied to. These factors induce errors in the measured quantities, and although quantum error correction schemes have been devised decades ago [41,42], their implementation is hindered by the fact that they require additional qubits to correct the error on a single qubit, making them impractical for NISQ-era devices with a limited number of available qubits (typically of the order of 6–10). A recent alternate approach exploits the available qubits but repeats the experiments for a different number of times, and with different sets of quantum gates. The resulting data can be extrapolated to the case when there is no noise affecting the experiment, assuming a general noise model. This approach, known as the zero-noise extrapolation (ZNE), has been intensively investigated in Refs. [43–49]. It falls into the category of error mitigation rather than error correction. Schemes for addressing depolarizing errors have been investigated in Ref. [50], and readout errors in Refs. [51–53]. Proposals of correcting depolarizing noise in a hierarchical fashion in quantum circuits depending on whether they contribute to the UV or IR physics have been put forward in Ref. [54], and they would allow targeted improvements in scientific applications in appropriate energy windows.

Our main goal in this article is to present models and implement corresponding quantum circuits suitable for NISQ devices for simulating real-time dynamics in pure gauge theories on single and double plaquettes. The plaquette interaction has been considered before in Ref. [27] following the usual Wilson formulation of formulating lattice gauge fields, having an infinite-dimensional Hilbert space for each link degree of freedom. This necessarily needs a truncation in the allowed set of states to be represented in an architecture with a finite number of qubits. Instead, we will consider a different formulation of lattice gauge theories, which are commonly known as quantum link models (QLMs) [55–57]. This formulation is ideally suited for implementation in quantum computers, since gauge invariance is realized exactly with a finite-dimensional Hilbert space for each link degree of freedom. In fact, the dimensionality of the local Hilbert space can be tuned in a gauge-invariant manner.

The strength of QLMs for NISQ devices is illustrated quantitatively in Table I (see Appendix C in the Supplemental Material for more details [58]), where the minimum number of two-qubit gates needed per qubit to simulate a single Trotter step of the time evolution of gauge theory potential terms is given for QLMs as well as truncated Wilson theories. A d-dimensional square lattice is assumed, and the circuit implementation used is the one we use in our simulations, and is described in Sec. III. The Wilson column refers to the potential terms of the Kogut-Susskind Hamiltonian [59–61], and the Improved Wilson

TABLE I. The number of two-qubit gates necessary for each qubit that corresponds to a link, for a single Trotter step and as a function of square lattice dimension d. Details are in Appendix C of the Supplemental Material [58].

Gauge group	QLM	Wilson	Improved Wilson
$\mathbb{Z}_2$	$2(2d-2)$	$2(2d-2)$	$2\times 3(2d-2)+2(2d-4)(2d-2)$
$U(1)$	$16(2d-2)$	$2\times 2048(2d-2)$	$2\times 32\times 4096\times 3(2d-2)+2\times 32\times 4096\times (2d-4)(2d-2)$

column is for the Symanzik correction terms which have been proposed to reduce the number of Trotter steps necessary for a simulation [59,62]. While the Kogut-Susskind Hamiltonian and the Symanzik improvement have the prospect of being very useful for simulating gauge theories in the future of quantum computing, Table I makes it clear that quantum link models are much more suited for taking the first steps of simulating time evolution for gauge theories on real hardware, with the aforementioned advantage of being gauge invariant at every tuning step. In fact, even exactly gauge-invariant QLMs of non-Abelian theories are in much closer reach for time evolution than alternative formulations—for example, an $SO(3)$-symmetric theory would require $162(2d-2)$ two-qubit gates per qubit per Trotter step [57,63].

QLMs are quite popular for implementation on analog quantum simulators [16,18,19], and it makes sense to develop the corresponding implementation in digital platforms as well. Initial studies of the construction of quantum circuits for the plaquettes using the QLM approach were reported in Refs. [64,65]. We focus on the theories with $\mathbb{Z}_2$ and $U(1)$ local symmetries and explore their formulations on triangular and square lattice geometries. The Hamiltonians with these local symmetries have been used to describe physical systems in condensed matter and quantum information [66–68]. A quantum circuit for a triangular $U(1)$ quantum link model has been proposed in Ref. [69] and tested with classical hardware. Another recent work dealing with the triangular $U(1)$ quantum link model used dualization to obtain dual quantum height variables, which allows a denser encoding in terms of qubits [70]. To the best of our knowledge, our article is the first to demonstrate a hardware-independent error mitigation technique for the real-time evolution of quantum link lattice gauge theories.

The rest of the paper is organized as follows: In Sec. II, we describe the Hamiltonians, as well as the corresponding local unitary Abelian transformations which keep the Hamiltonian invariant, showing the constrained nature of the Hilbert space in these models. In Sec. III, we describe the quantum circuit used to implement the Hamiltonian interactions and perform the real-time dynamics. We outline the methodology we adopted in mitigating the errors due to decoherence and readout in Sec. IV, and we outline the experimental results obtained in Sec. V. Finally, we discuss possibilities of extending this study to larger lattice dimensions, as well as to non-Abelian gauge theories in Sec. VI.

II. ABELIAN LATTICE GAUGE THEORY MODELS

In this section, we discuss the quantum Hamiltonians, which are invariant under local $\mathbb{Z}_2$ and the $U(1)$ transformations. The gauge theory Hamiltonians are characterized by the plaquette term, which is the simplest gauge-invariant operator that can be constructed.

A. The $\mathbb{Z}_2$ gauge theory

Consider a square lattice, for which the smallest closed loop would be a plaquette containing the four links around an elementary square. Through a four-spin interaction involving $S^z = \sigma^z/2$ operators, and a single-spin $S^x = \sigma^x/2$ operator on each of the links, we can realize the $\mathbb{Z}_2$ gauge theory Hamiltonian:

$$H = -g\sum_{\Box} U_{\Box} - \Gamma\sum_i S_i^x, \tag{1}$$

$$U_{\Box} = S^z_{r,\mu}S^z_{r+\mu,\nu}S^z_{r+\nu,\mu}S^z_{r,\nu}. \tag{2}$$

The gauge symmetry arises due to the invariance of the Hamiltonian under local unitary transformations according to the operator

$$\begin{aligned} V_r &= \sigma^x_{r,\mu}\sigma^x_{r,\nu}\sigma^x_{r-\mu,\mu}\sigma^x_{r-\nu,\nu} \\ &= \exp\left[i\pi\sum_{\mu}(S^x_{r,\mu} - S^x_{r-\mu,\mu})\right]. \end{aligned} \tag{3}$$

This can be directly proven from the fact that the Hamiltonian commutes with the local operator V_r, which is known as the Gauss law operator. This commutation relation $[U_{\Box}, V_r] = 0$ follows from a few lines of algebra.

The eigenstates of the Hamiltonian are classified into two super-selection sectors according to $V_r|\psi\rangle = \pm 1|\psi\rangle$ in the computational basis of σ^x. For a square lattice, four links touch a single vertex, and 2^4 spin configurations are possible, but only half of them have $V_r = 1$ and the other half $V_r = -1$, giving rise to two superselection sectors.

We are interested in implementing the real-time evolution of simple plaquette models on superconducting-qubit-based IBM Q quantum computers. For our purposes, we can work in the σ^x basis, where the Gauss law as well as the Γ term in the Hamiltonian are diagonal. We aim to start with initial product states in the σ^x basis, which is then evolved by an off-diagonal plaquette Hamiltonian. We note that the Γ term not only contributes a diagonal term in this basis but

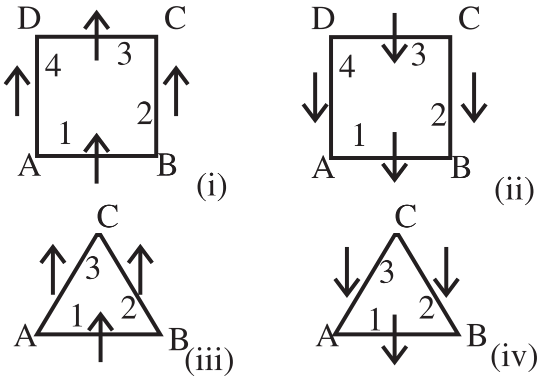

FIG. 1. Basis states of the $\mathbb{Z}_2$ gauge theory in the S^x basis for both the square plaquette (upper row) and the triangular plaquette (lower row). The configurations (i) and (ii) satisfy the Gauss law $V_r = 1$ at all sites for the square, and the configurations (iii) and (iv) satisfy $V_r = 1$ at all sites for the triangular plaquette.

would also be zero for certain Gauss law sectors for the single-plaquette system. We choose $\Gamma = 0$ for the experiments performed on the quantum computer.

For the single-plaquette system shown in Fig. 1 (top row) with four links in all and two links touching each vertex (labeled as A, B, C, and D), we start by explicitly writing the Hamiltonian and the Gauss law:

$$H = -g S_1^z S_2^z S_3^z S_4^z,$$
$$V_A = \sigma_1^x \sigma_4^x; \quad V_B = \sigma_1^x \sigma_2^x; \quad V_C = \sigma_2^x \sigma_3^x; \quad V_D = \sigma_3^x \sigma_4^x. \tag{4}$$

For a single plaquette, 16 states are possible in total, which comprise the full Hilbert space. We construct the Hamiltonian in each of the sectors characterized by particular local values of the Gauss law. Since this a $\mathbb{Z}_2$ theory, the Gauss law can only take ± 1 values. The two states illustrated in the top row of Fig. 1 have $V_x|\psi\rangle = 1|\psi\rangle$ at each site. Similarly, it is possible to obtain two configurations which have $V_x|\psi\rangle = -1|\psi\rangle$ at each site. Furthermore, it is possible to place two positive and two negative $\mathbb{Z}_2$ charges, giving rise to six more sectors. Each sector has two states which are related to each other by charge conjugation (global $S^x \leftrightarrow -S^x$ flip).

For our purposes, we consider the quench dynamics within the sector $(V_A, V_B, V_C, V_D) = (+,+,+,+)$. The Hamiltonian is two-dimensional in this sector with the eigenstates

$$|\Psi_1\rangle = (|1111\rangle + |0000\rangle)/\sqrt{2},$$
$$|\Psi_2\rangle = (|1111\rangle - |0000\rangle)/\sqrt{2}. \tag{5}$$

Here, the notation $|0000\rangle$ denotes all spins aligned in the $+1$ direction of the S^x (computational) basis, and $|1111\rangle$ denotes all spins aligned in the -1 direction. Similarly, for the $(-,-,-,-)$ sector, we get

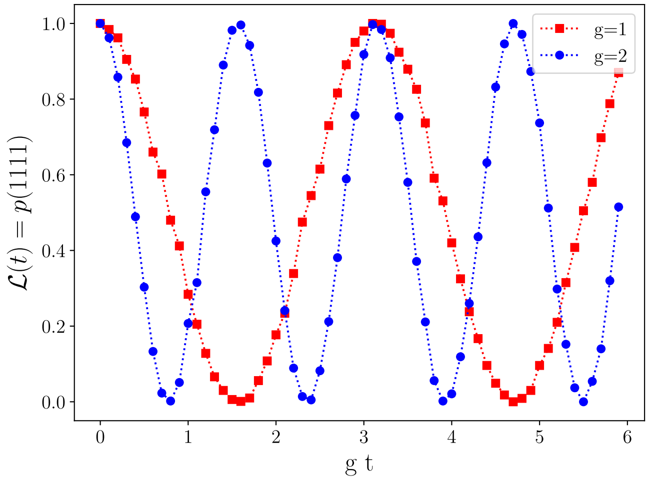

FIG. 2. Oscillations of the Loschmidt probability $\mathcal{L}(t) = p(1111)$ for the square $\mathbb{Z}_2$ plaquette on the ibmq_qasm_simulator, which is a general-purpose simulator. The points are the points from the simulator, and the line is provided only to guide the eye. The system has a two-dimensional gauge-invariant Hilbert space, and there is a two-state Rabi oscillation when started from the state $|1111\rangle$ to the state $|0000\rangle$. An identical behavior is also observed in the triangular $Z(2)$ plaquette. Increasing the coupling by a factor of 2 is identical to speeding up the dynamics by a factor of 2.

$$|\Psi_3\rangle = (|1010\rangle + |0101\rangle)/\sqrt{2},$$
$$|\Psi_4\rangle = (|1010\rangle - |0101\rangle)/\sqrt{2}. \tag{6}$$

Again, the 0's and 1's denote spins aligned in the $+1$ and -1 directions of the S^x basis, respectively. The real-time evolution starting from an initial state $|1111\rangle$ is therefore a two-state Rabi oscillation. A useful quantity to measure is the return, or the Loschmidt probability, defined as the projection of the time-evolved initial state onto the initial state:

$$\mathcal{L}(t) = |\mathcal{G}(t)|^2; \qquad \mathcal{G}(t) = \langle\psi_0|e^{-iHt}|\psi_0\rangle. \tag{7}$$

In Fig. 2, we show the return or the Loschmidt probability, which is an indicator for the so-called dynamical quantum phase transitions [71]. As shown in the figure, increasing the frequency is equivalent to speeding up the dynamics by the same factor.

It is also possible to consider the $\mathbb{Z}_2$ gauge theory on different lattices, such as the triangular, hexagonal, or the checkerboard lattice. Here we will also consider the example of a triangular lattice. Again, considering a single plaquette as illustrated in Fig. 1 (bottom row), there are three links in a plaquette, and each vertex contains two links where the Gauss law can be imposed. In this case, labeling the three vertices as A, B, and C; and the three links as 1, 2, and 3, the Hamiltonian and the Gauss law are

$$H = -g S_1^z S_2^z S_3^z,$$
$$V_A = \sigma_1^x \sigma_2^x; \qquad V_B = \sigma_2^x \sigma_3^x; \qquad V_C = \sigma_3^x \sigma_1^x. \tag{8}$$

The analysis of the triangular plaquette is also similar to that of the square plaquette, leading to two quantum states in each Gauss law sector (and four sectors total), and thus the real-time evolution also displays a characteristic Rabi oscillation similar to the one in the square plaquette.

In the following sections, we study both plaquette models on a quantum hardware, where decoherence will cause mixing among the different sectors. The extent of the mixing can help us to understand the (in)efficiency of the quantum hardware and which optimizations, error corrections, or mitigations are likely to help.

B. The U(1) quantum link model

We next consider the case of the $U(1)$ lattice gauge theory, which has considerably richer physics—and as a stepping stone to studying QED, has relevance to the fundamental physics of nature. We will consider the theory on both the square and the triangular lattice, as in the case of the $\mathbb{Z}_2$ theory. The phase diagrams of both systems have been studied in the literature [70,72], as well as aspects of dynamics and thermalization of the model on the square lattice [73] and its potential realization on analog and digital computers [74–76]. Since we want to implement the models using actual quantum hardware, we will consider very small systems involving single and double plaquettes, as shown in Fig. 3.

To implement a local $U(1)$ symmetry for the Hamiltonian in a simple way, we need the spin-raising and -lowering operators, given by $U_l = S_l^+ = \frac{1}{\sqrt{2}}(\sigma_l^x + i\sigma_l^y)$ and $U_l^\dagger = S_l^- = \frac{1}{\sqrt{2}}(\sigma_l^x - i\sigma_l^y)$. The operators U_l (and $U_l^\dagger$) are canonically conjugate to the electric flux operator living on the same link, $E_l = S_l^z$, and they obey the following commutation relations:

$$[E, U] = U; \qquad [E, U^\dagger] = -U^\dagger; \qquad [U, U^\dagger] = 2E. \tag{9}$$

Operators residing on different links always commute. With these operators, we can now define the lattice $U(1)$ Gauss law:

$$G_x = \sum_\mu (E_{x,\mu} - E_{x-\mu,\mu}). \tag{10}$$

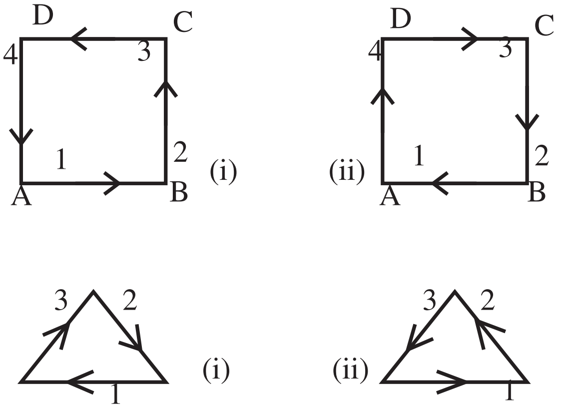

FIG. 3. Sample basis states for the square (top) and triangular (bottom) plaquettes of the $U(1)$ QLM, where the spins are quantized in the σ^z basis. For the square lattice, the spins pointing up (down) indicated by arrows on the vertical links correspond to $E = +\frac{1}{2}(-\frac{1}{2})$. For the links along the x axis (the horizontal links), the arrows pointing to the right (left) indicate spins quantized along $E = +\frac{1}{2}(-\frac{1}{2})$. For the triangular plaquette, the arrows pointing in the clockwise (counterclockwise) direction indicate spins quantized along $E = +\frac{1}{2}(-\frac{1}{2})$. Each of these examples of the basis states are in the $G_x = 0$ sector, which can be seen physically from the fact that every point has one arrow coming in and another going out.

Note that μ denotes the lattice unit vectors, and thus for the square lattice, $\mu = 1, 2$; while for the triangular lattice, $\mu = 1, 2, 3$. This operator G_x generates the gauge transformations, which can be expressed as $V = \prod_x \exp(-i\alpha_x G_x)$, where α_x is the (local) parameter associated with the local unitary transformation. This operator commutes with the plaquette Hamiltonian defined on the entire lattice. For the square lattice, the local Hamiltonian involves four links around a plaquette, and the model has the form

$$H_\square = -g \sum_\square (U_\square + U_\square^\dagger),$$
$$U_\square = S^+_{r,\mu} S^+_{r+\mu,\nu} S^-_{r+\nu,\mu} S^-_{r,\nu}, \tag{11}$$

where μ, ν are the lattice axes and r is the bottom-left corner of a square plaquette. For the triangular lattice, the three-link plaquette Hamiltonian has the form

$$H_\triangle = -g \sum_\triangle (U_\triangle + U_\triangle^\dagger),$$
$$U_\triangle = S^+_{xy} S^+_{yz} S^+_{zx}, \tag{12}$$

where the points x, y, z are the vertices of a triangle. Mathematically, the commutation relation $[G_x, H] = 0$ ensures that the Hamiltonian is invariant under local unitary transformations $H = VHV^\dagger$, resulting in a highly constrained system.

From these equations, the single-plaquette case can be obtained by only keeping the links that exist in the triangle or the square geometry, and gives rise to

$$H_\square = -g(S_1^+ S_2^+ S_3^- S_4^- + S_1^- S_2^- S_3^+ S_4^+),$$
$$H_\triangle = -g(S_1^+ S_2^+ S_3^+ + S_1^- S_2^- S_3^-), \tag{13}$$

with Gauss law operators given by

$$\begin{aligned} G_A &= S_4^z + S_1^z, \qquad G_B = S_2^z - S_1^z, \\ G_C &= -S_2^z - S_3^z, \qquad G_D = S_3^z - S_4^z \end{aligned} \tag{14}$$

for the square plaquette, and

$$G_A = S_1^z - S_3^z, \quad G_B = S_2^z - S_1^z, \quad G_C = S_3^z - S_2^z \tag{15}$$

for the triangular plaquette, where the link subscripts correspond to the labels in Fig. 3. Note that the conventions for the signs of the electric flux are given in the caption of the figure.

For our purposes, it is useful to further simplify Eq. (13) and express the Hamiltonian in terms of the Pauli matrices, which will allow us to construct the quantum circuits using the circuit identities introduced in the next section. For the square plaquette, we obtain

$$\begin{aligned} H_\square = -\frac{g}{2}[&\sigma_1^x\sigma_2^x\sigma_3^x\sigma_4^x + \sigma_1^y\sigma_2^y\sigma_3^y\sigma_4^y - \sigma_1^x\sigma_2^x\sigma_3^y\sigma_4^y \\ &- \sigma_1^y\sigma_2^y\sigma_3^x\sigma_4^x + \sigma_1^y\sigma_2^x\sigma_3^y\sigma_4^x + \sigma_1^y\sigma_2^x\sigma_3^x\sigma_4^y \\ &+ \sigma_1^x\sigma_2^y\sigma_3^y\sigma_4^x + \sigma_1^x\sigma_2^y\sigma_3^x\sigma_4^y]. \end{aligned} \tag{16}$$

Thus, there are eight terms for a single plaquette when expressed with the Pauli matrices. For the triangular plaquette, we have four independent plaquette terms which have to be implemented in a quantum circuit:

$$H_\triangle = -g/\sqrt{2}[\sigma_1^x\sigma_2^x\sigma_3^x - \sigma_1^y\sigma_2^y\sigma_3^x - \sigma_1^y\sigma_2^x\sigma_3^y - \sigma_1^x\sigma_2^y\sigma_3^y]. \tag{17}$$

The solution of the single-plaquette problem is straightforward: for the $U(1)$ system as defined here, it is more natural to consider the system quantized in the σ^z basis (instead of the σ^x basis used in the $\mathbb{Z}_2$ case), such that the spin-up and the spin-down can be denoted by arrows pointing in and pointing out from a given site, respectively. This can be interpreted physically as the plaquette operators raising or lowering states by a unit of magnetic field (which is like a clockwise or counterclockwise arrangement of the electric fluxes around the plaquette). For the triangular lattice, this means that there are only $2^3 = 8$ basis states, and the square lattice has $2^4 = 16$ such basis states. The Gauss law further selects only two basis states for each of the two lattices. For the triangular lattice with $G_x = 0$ everywhere as an example, we denote them as $|000\rangle$ and $|111\rangle$; while for the square lattice with $G_x = 0$ we denote them as $|0011\rangle$ and $|1100\rangle$. Note that 0 denotes a spin-up and 1 a spin-down in the σ^z basis. The states are shown in Fig. 3. The Hamiltonian for both cases is therefore a two-dimensional off-diagonal matrix. The two eigenstates are thus given by a symmetric and antisymmetric linear superposition of the two basis states. The real-time evolution—with the Loschmidt probability oscillating between the two basis states—is qualitatively the same as that given in Fig. 2—the period simply differs as a function of g.

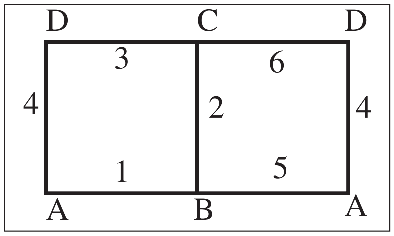

FIG. 4. The setup for two plaquettes which have periodic boundary conditions in the longer direction. The links are marked with numerals, while the sites are marked with letters.

C. Two-plaquette system

As one more test of the quantum hardware, we consider a two-plaquette system on a square lattice with periodic boundary conditions for the $\mathbb{Z}_2$ gauge theory. The geometry of the system is shown in Fig. 4. For clarity, let us explicitly write the Hamiltonian and the Gauss law for this case:

$$\begin{aligned} H &= -gS_1^zS_2^zS_3^zS_4^z - gS_5^zS_4^zS_6^zS_2^z, \\ G_A &= \sigma_1^x\sigma_4^x\sigma_5^x; \qquad G_B = \sigma_5^x\sigma_2^x\sigma_1^x; \\ G_C &= \sigma_6^x\sigma_2^x\sigma_3^x; \qquad G_D = \sigma_3^x\sigma_4^x\sigma_6^x, \end{aligned} \tag{18}$$

following the labeling in Fig. 4. Because the σ_{N}^z's commute with each other, the time evolution given by this Hamiltonian can be decomposed as the evolution given by the product of the time evolution given by each of the two terms for H in Eq. (18). This decomposition is exact and not subject to any Trotter errors. For each term, we can use the strategy to be described in the next section: introduce an ancillary qubit which couples to the rest of qubits in the plaquette, and perform dynamics with the help of the ancillary qubit. Further, the structure of the Gauss law implies that we can impose the constraint $G_x = 1$ for all the sites. Without the constraint, there are $2^6 = 64$ states. The Gauss law constraint will then reduce this number. For example, imposing $G_A = 1$ affects the spins on the links 1, 4, and 5. The only configurations allowed are those where either all three have $+1$ in the σ^x basis, or exactly two of the spins 1, 2, and 5 have -1 in the σ^x basis, and the third spin is $+1$.

While the solution of the two-plaquette system is worked out in Appendix B of the Supplementary Material [58] we summarize the relevant points for the simulation of quench dynamics of this system. The two-plaquette system in the sector $G_x = 1$ for all x has eight basis states. These eight states can be further divided into two sectors using the global winding number symmetry, which cuts the plaquettes horizontally and vertically.

For a general rectangular system with sizes $L_{\mathrm{x}} \times L_{\mathrm{y}}$, we can define a global winding number W_n for each of the spatial directions. If we draw a line at a fixed $x = x_0$ ($y = y_0$) along the y (x) direction, then this line cuts all horizontal (vertical) links [i.e., those pointing in the x (y) direction]. Denoting the set of spins on the line as $\{\sigma_m\}$, our winding number operator is given by

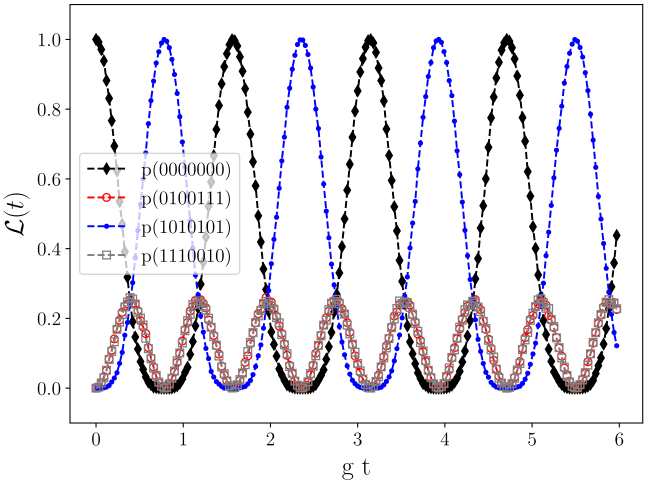

FIG. 5. Quench dynamics of the two-plaquette simulation from state 1 into states 2, 3, and 4, given by the ibmq_qasm_simulator. The Loschmidt probability oscillates between 0 and 1 for the states 1 and 3, while it oscillates between 0 and 0.25 for the states 2 and 4. Moreover, the probability oscillations between states 1 and 3 are exactly out of phase, as in the two-state systems considered previously, but they have equal projections into states 2 and 4. As before, the points are the ones from the simulator, and the dashed line only guides the eye.

$$W_n = \prod_m \sigma^x_m, \tag{19}$$

where $n = y$ if $m = x$, and vice versa. For our case, the expressions for the operators are

$$W_x = \sigma^x_4\sigma^x_2; \quad W_y(13) = \sigma^x_1\sigma^x_3; \quad W_y(56) = \sigma^x_5\sigma^x_6. \tag{20}$$

The last two expressions for W_y are actually the same, as can be seen by using the Gauss law for the sites. Thus, in a perfect implementation, only four basis states entangle with each other under a unitary evolution. In Fig. 5, we show the Loschmidt probability for starting in one of these states, and the oscillations into the other three states. This system thus provides a good playground for tuning quantum hardware to reproduce these involved oscillations, as well as benchmarking to what extent local and global symmetries can be preserved in these circuits.

For completeness, we consider the $U(1)$ theory on two plaquettes—the entire Hamiltonian would have a total of 16 terms, which, when represented by the quantum gates, are

$$\begin{aligned} H = -\frac{J}{2}[&\sigma^x_1\sigma^x_2\sigma^x_3\sigma^x_4 + \sigma^y_1\sigma^y_2\sigma^y_3\sigma^y_4 - \sigma^x_1\sigma^x_2\sigma^y_3\sigma^y_4 \\ &- \sigma^y_1\sigma^y_2\sigma^x_3\sigma^x_4 + \sigma^y_1\sigma^x_2\sigma^y_3\sigma^x_4 + \sigma^y_1\sigma^x_2\sigma^x_3\sigma^y_4 + \sigma^x_1\sigma^y_2\sigma^y_3\sigma^x_4 \\ &+ \sigma^x_1\sigma^y_2\sigma^x_3\sigma^y_4 + \sigma^x_5\sigma^x_4\sigma^x_6\sigma^x_2 + \sigma^y_5\sigma^y_4\sigma^y_6\sigma^y_2 - \sigma^x_5\sigma^x_4\sigma^y_6\sigma^y_2 \\ &- \sigma^y_5\sigma^y_4\sigma^x_6\sigma^x_2 + \sigma^y_5\sigma^x_4\sigma^y_6\sigma^x_2 + \sigma^y_5\sigma^x_4\sigma^x_6\sigma^y_2 \\ &+ \sigma^x_5\sigma^y_4\sigma^y_6\sigma^x_2 + \sigma^x_5\sigma^y_4\sigma^x_6\sigma^y_2]. \end{aligned} \tag{21}$$

These terms do not all commute with each other, so Trotterization would be necessary to simulate their real-time evolution. In this paper, we only consider the $\mathbb{Z}_2$ case which involves no Trotter steps.

III. QUANTUM HARDWARE AND CIRCUITS

In our plaquette model simulations, we make use of IBM Q hardware, which is based on superconducting (transmon) qubits. We discuss below a few details on how we work with this NISQ hardware, both in terms of selecting the platform for each experiment and in terms of circuit implementation.

A. Hardware selection

Superconducting qubits have the advantage of being relatively fast at running experiments compared to trapped-ion qubits, but the disadvantage of relatively short decoherence times [77].

Because of this, the topology of the circuits is important, as it will make a difference for how many gates are necessary to realize a particular simulation. Figure 6 shows three real-hardware topologies that are used in this paper. For each experiment, we may select hardware depending on optimal topology.

Another important consideration for choosing hardware is the *quantum volume* of the device, which is generally a measure of the most complex circuit that can compute accurate quantities according to a particular threshold for a given device. IBM Q measures quantum volume using the following formula:

$$V_Q = 2^{\min(d,m)}, \tag{22}$$

where d is the depth of the circuit (measured according to two-qubit gates), and m is the number of qubits, so that $\min(d, m)$ tells us the largest square circuit possible that still meets the set accuracy threshold [78]. The IBM Q devices each have a V_Q measured, and so in our experiments we favor using those with the higher V_Q values.

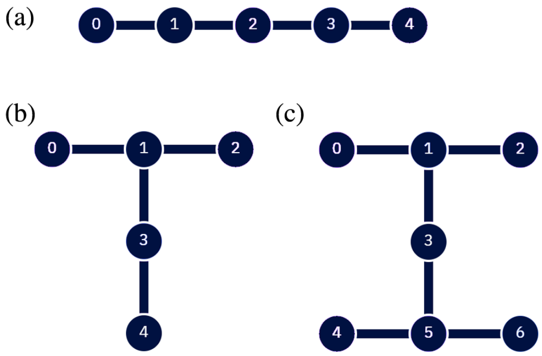

FIG. 6. Three circuit topologies used for the simulations. Images taken from IBM Quantum Experience.

Specifically, the devices used to obtain our results include IBM Q Valencia and IBM Q Quito, which each have $V_Q = 16$, as well as IBM Q Bogota, IBM Q Santiago, and IBM Lagos, which each have $V_Q = 32$.

B. Circuit implementation and scaling

The real-time simulation of plaquette dynamics involves realizing Hamiltonians of several spins on a plaquette. A very simple case looks like

$$H_{\mathrm{N}} = -g\sigma^3_{xy}\sigma^3_{yz}\sigma^3_{zw}\sigma^3_{wx}, \tag{23}$$

where $\mathrm{N} = 4$ and the sites x, y, z, w are corners of a square plaquette. To realize a real-time evolution with the above Hamiltonian, we implement the following gate sequence [64,65]:

$$U_{\mathrm{S,A}}(t) = \exp\left[i\frac{\pi}{4}\sigma^3_{\mathrm{A}}\sum_{j=1}^{N}\sigma^3_j\right]\exp\left[igt\sigma^1_{\mathrm{A}}\right] \times \exp\left[-i\frac{\pi}{4}\sigma^3_{\mathrm{A}}\sum_{j=1}^{N}\sigma^3_j\right]. \tag{24}$$

A proof of Eq. (24) is detailed in Appendix A of the Supplementary Material [58].

This identity has the nice property of being applicable to plaquettes that contain a general number of spins, N, and in all cases it allows for the time-evolution portion to be performed entirely on a single extra spin, which we label with the index A. This spin is in addition to the N spins that make up the plaquette, and is known as *ancillary.* In principle, for a quantum circuit implementation (where we represent each spin with a qubit), one would only need one ancillary qubit for the entire system, but due to topological issues it may be more efficient in terms of circuit depth to add more ancillary qubits in systems with more plaquettes. Still, with at most one ancillary qubit per plaquette, the number of qubits needed for simulation scales linearly with the number of links in the system.

If all terms in the Hamiltonian commute, the number of gates needed is constant as a function of real time, but in the more generic case where the terms do not commute and so Trotterization is necessary, the circuit depth scales linearly with time. In our examples below, we focus only on cases where no Trotterization is needed.

IV. ERROR MITIGATION METHODOLOGIES

As mentioned earlier, one major practical obstacle to developing physical devices to perform quantum computations is the significant inherent noise that affects NISQ quantum devices. In theory, quantum error correction is possible by encoding the information of the desired circuit into a highly entangled state composed of a very large number of physical qubits [41,42]. However, this large number of qubits makes the hardware requirements too demanding to be implemented in practice (although promising results point in the right direction [79]). An alternative is to take advantage of systematic and reproducible properties of the hardware. These properties are exploited as part of the so-called error mitigation schemes, which have proven to be successful in NISQ-era devices [43–49,51–53,80]. Among these, we consider two types: readout error mitigation and zero noise extrapolation (ZNE), which aim to reduce noise coming from two different sources: readout and gate operation decoherence. We emphasize that while here we use these techniques on IBM Q hardware, they are in fact hardware-agnostic techniques—they rely only on the set of gates available and do not rely on the details of the hardware such as the type of qubits used—and therefore can be used to improve results on any universal quantum device.

A. Readout error mitigation

One important source of errors are the so called "readout" errors, which arise due to the comparable measurement and decoherence times [51–53,81]. This can cause undesired state decays, affecting the state captured in the measurement. Assuming a classical stochastic model for the noise-affecting measurements, the statement of the problem can be formulated by using the response matrix $P(m|t)$, which connects a noisy measurement m to the true/ideal measurement t by the relation $m = Pt$. Naively, one can use the inverse of the response matrix to obtain $t = P^{-1}m$ and recover the true value of the measurement. The problem then consists in performing a series of calibration experiments to measure P, and then using it to recover t given m in subsequent independent experiments.

Packages such as `qiskit-ignis` [82] are based on the response matrix formulation of the readout error mitigation scheme, but (by default) do not try to compute P^{-1} directly by matrix inversion. Instead, t is recovered by finding the minimum of the least squares expression:

$$f(t) = \sum_{i=1}^{2^n}(m_i - (P\cdot t)_i)^2, \tag{25}$$

where n is the total number of qubits in the circuit. This methodology is more robust than matrix inversion for general NISQ hardware [52,82]. More involved methods combine the previous approach with gate inversion to further improve the error mitigation results [53], while unfolding methods have also been proposed and tested in the literature [52].

In most cases, the ability to apply readout error mitigation is limited by the number of qubits (n) in the circuit, as the number of calibration experiments required to evaluate P grows as 2^n. Moreover, the calibration step of estimating P is hardware dependent and needs to be performed immediately before running the experiments to

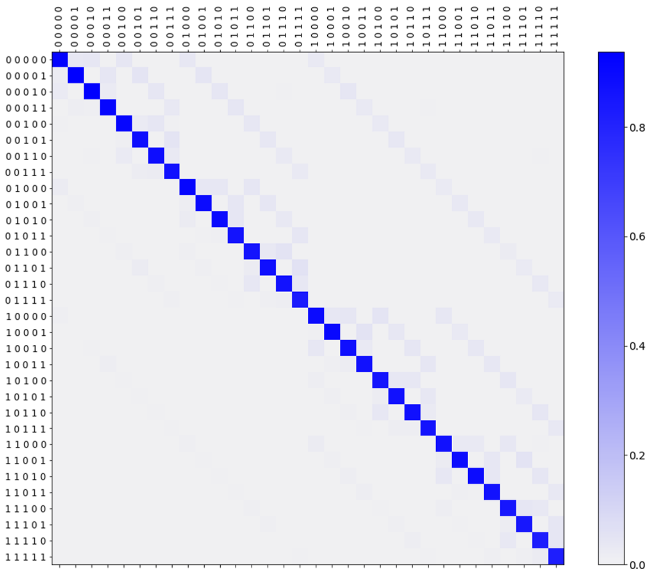

FIG. 7. Response mitigation matrix computed by `ignis` for IBM Q Manila (five-qubit system).

guarantee that temporal deviations in the particular hardware are accounted for. An real-hardware example of the response matrix obtained for a five-qubit system (IBM Q Manila) using `ignis` is shown in Fig. 7. As expected, the diagonal entries have probability values close to 1, but there is still significant drift toward nondiagonal entries. As presented and discussed in Sec. V, correcting for these small deviations resulted in significant improvements in the final mitigated data.

Clearly, going beyond circuits with a small number of qubits would be prohibitively expensive due to the number of experiments required to evaluate the response matrix. Some proposals have considered the possibility of assuming close to uncorrelated readout errors between the qubits, which would drastically reduce the number of experiments required [81]. Studying these potential improvements goes beyond the scope of this work.

B. Corrections against decoherence: *Mitiq*

The second source of error comes from the gate portion of the circuit before measurements occur. Longer circuits will consist of more gates, and both the longer runtimes and the gate implementation (transmon qubits in the case of the IBM Q devices) will cause additional errors to pile up. To mitigate this source of error, we use a method known as zero-noise extrapolation (ZNE), where we introduce additional noise in a controlled way in order to empirically develop a noise model that we can extrapolate to the zero-noise case.

Implementations of ZNE include those that involve pulse control and run multiple experiments with pulses of different durations [44], and those that involve *folding*, which consists of insertions of additional gate identities to the circuit which would not change the results in an ideal simulation, but will make results on real hardware more noisy. This information on how the gates affect the noise level can then be used to develop a noise model and extrapolate back to an "ideal" result.

We used the folding option in this paper, and specifically we used the *Mitiq* package to implement it [46]. As an example, Fig. 8 shows two equivalent circuits, but the second circuit has three extra identity insertions, each consisting of two identical CNOT gates in a row. Because the error rates of the two-qubit CNOT gates are significantly higher than those for the single-qubit gates (roughly 10 times different on IBM Q devices), we will assume perfect fidelities for the single-qubit gates and model all the error coming from the two-qubit gates (an option within *Mitiq*). With this in mind, because circuit a in Fig. 8 has ten CNOT gates, and circuit b has sixteen CNOT gates, the scale factor of circuit b is 1.6 times that of circuit a.

Figure 9 shows real-hardware examples of different extrapolations for several circuits, with the ideal result for each (determined using a simulator) marked at scale factor "0." The first row shows example extrapolations for the $\mathbb{Z}_2$ model on the square plaquette at two different times

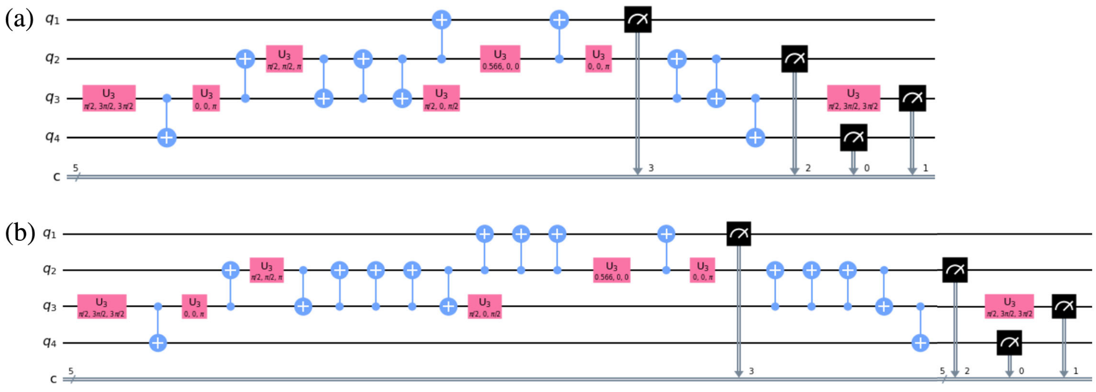

FIG. 8. An example of using the *Mitiq* package for folding a circuit that gives the time evolution of the $Z(2)$ gauge theory on a triangular plaquette. Both circuits are equivalent, but the second one contains additional identity insertions of CNOT gates such that when measured using the CNOT circuit depth, the second circuit is 1.6 times longer than the former.

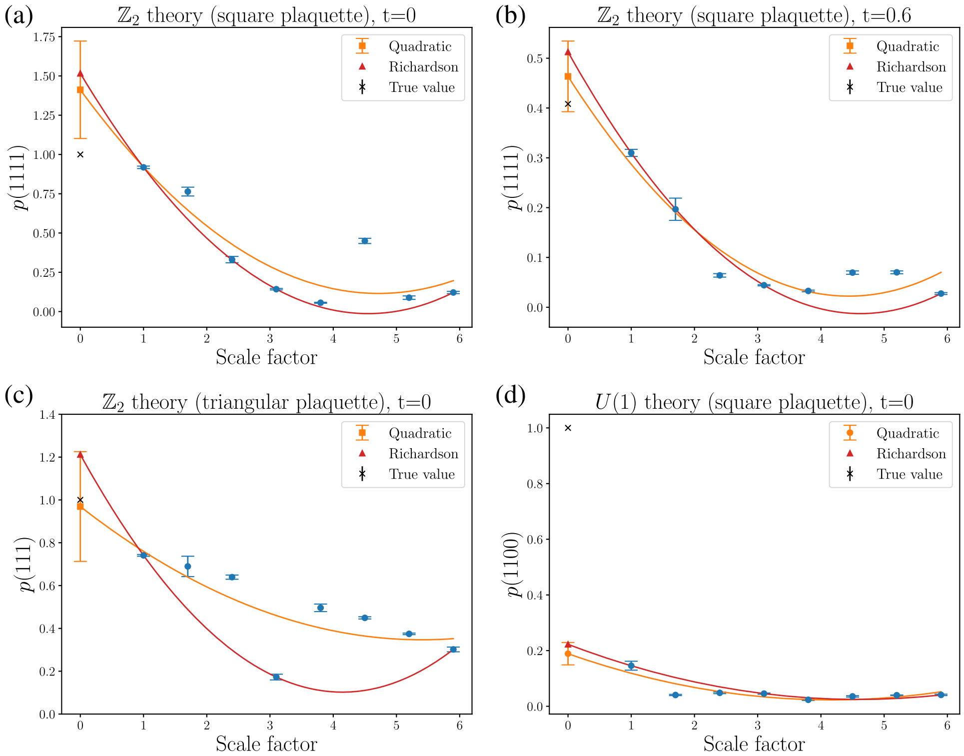

FIG. 9. The plots in the top row show zero-noise extrapolation for the $\mathbb{Z}_2$ theory on a square plaquette (IBM Q Valencia hardware) at two times: (a) $t = 0$ and (b) $t = 0.6$. The bottom row shows zero-noise extrapolation for (c) the $\mathbb{Z}_2$ gauge theory on a triangular plaquette (IBM Q Bogota) at $t = 0$, and (d) a U(1) gauge theory on a square plaquette (IBM Q Quito) at $t = 0$.

in the evolution. The bottom-left image shows an extrapolation at $t = 0$ for the $\mathbb{Z}_2$ theory on the triangular plaquette, and the bottom-right image shows one at $t = 0$ for the U(1) theory on the square plaquette. The two extrapolations shown are a quadratic fit and a Richardson extrapolation, explained in Kandala *et al.* [44]. From this empirical data, we decided to use the quadratic extrapolation for our data, as it appeared less susceptible to experimental outliers (such as those in the bottom left of Fig. 9).

It is interesting to note the presence of two regimes which display sensitivity to a change in the circuit depth. For larger scale factors which exceed the quantum volume of the system, the dependence on the scale factor becomes insensitive. At $t = 0$, the measurements for increasing the circuit length decay only slowly until the scale factors exceed 3 for the $\mathbb{Z}_2$ model, and about 6 for the $U(1)$ model. For $t = 0.6$, this decay is much faster for the $U(1)$ model than the $\mathbb{Z}_2$ model. Typically, the $U(1)$ circuit is significantly more entangled, and it becomes more so when the extrapolation is attempted at finite t.

V. RESULTS

This section gives our real-time evolution results for the Loschmidt probability, as well as observables G_x and W_y for plaquette simulations on NISQ hardware. In each simulation, we take five measurements (8192 shots per measurement) at every point in time and at each of the eight different scale factors illustrated by Fig. 9. This allows us to get error bars and perform ZNE at every time. For each time, the different scale factor measurements were all taken within the same calibration: see Appendix D in the Supplemental Material for a note about the fluctuations of the measurements across different calibrations of the IBM Q hardware [58]. Each simulation consists of 20 points in time total, leading to $5 \times 8 \times 20 = 800$ circuit measurements to produce the error mitigated plots for a theory on a particular plaquette.

A. $\mathbb{Z}_2$ theory on single plaquettes

We first discuss the results for the $\mathbb{Z}_2$ theory on square and triangular plaquettes, which were simulated on IBM Q Valencia and IBM Q Bogota, respectively. The results are plotted in Fig. 10. Figures 10(a) and 10(b) in the top row show a simulation of a single square-plaquette system for two different couplings: $g = 1.0$ and $g = 2.0$. We chose IBM Q Valencia for this simulation because of its T-shaped topology, illustrated in Fig. 6(b), which reduced the circuit depth necessary, since the ancillary qubit could be placed at a junction directly connected to three other qubits. There was other hardware available with better V_Q (32 versus 16 for Valencia), but the topological advantage of the T-shaped hardware made for better results despite the worse V_Q.

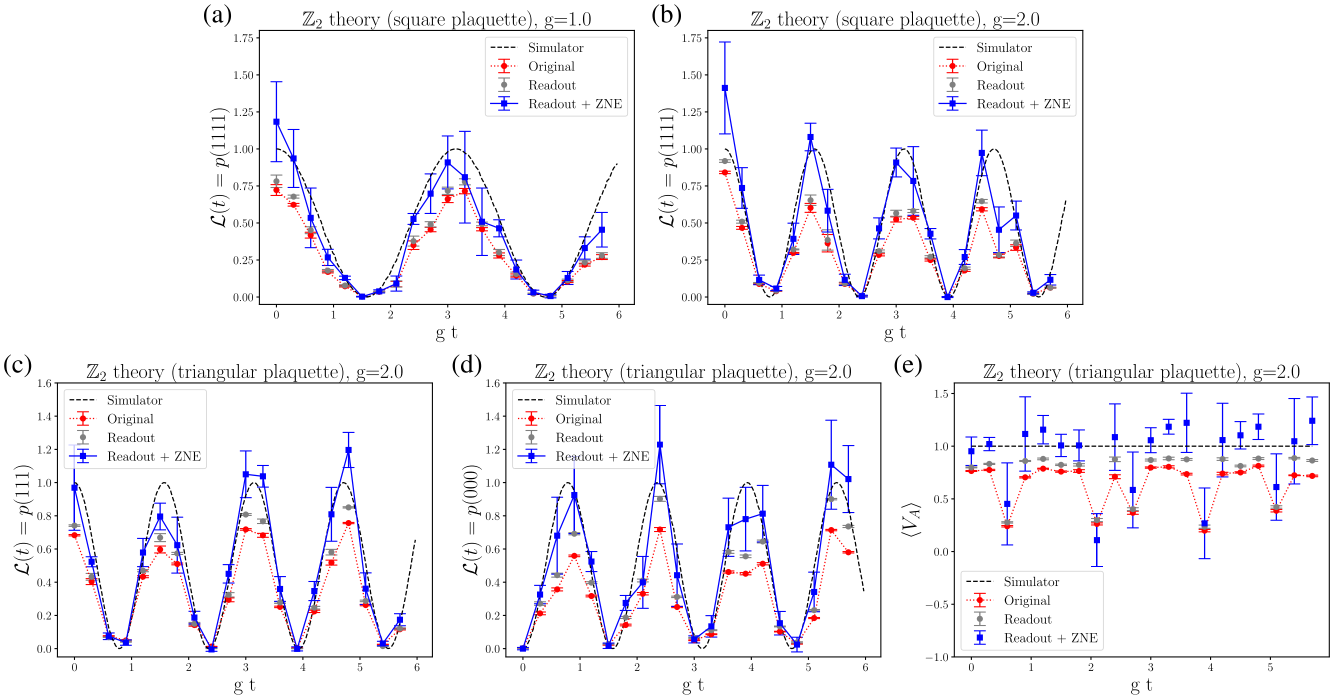

FIG. 10. Real-time evolution of the $\mathbb{Z}_2$ theory on a single plaquette. Plots (a) and (b) in the first row show the Loschmidt probability data for a square plaquette on IBM Q Valencia (with two couplings: $g = 1.0, 2.0$); then plots (c) and (d) show the Loschmidt probability data for a triangular plaquette on IBM Q Bogota. Finally, plot (e) shows the Gauss law observable V_A, which means the observable involving the links 1 and 2, as shown in Fig. 1.

In these plots, we give the ideal simulator measurement of the Loschmidt probability in addition to the original (raw) data from the circuit, followed by the readout error correction, followed by the readout and ZNE error corrections in combination. Here we see that with both these corrections, we are able to get to the correct simulator measurements within errors.

The next two plots, Figs. 10(c) and 10(d) in the bottom row of Fig. 10, give the results for a $\mathbb{Z}_2$ theory on a triangular plaquette instead. Here, a smaller circuit depth is needed as compared to the square plaquette, so we use IBM Q Bogota due to its better quantum volume [it has a linear topology, as seen in Fig. 6(a)]. These plots give the time evolution for the two states in the $V_A = V_B = V_C = 1$ sector: $|000\rangle$ and $|111\rangle$, and one can see from the simulator lines that their probabilities always add up to 1. As in the case for the $\mathbb{Z}_2$ theory on the square plaquette, the error mitigation methods allow for the fully mitigated data to track the simulator data within error bars. The last plot, Fig. 10(e), in the lower-right corner of Fig. 10, is a measure of how well the circuits for the system on the triangular plaquette are producing only states that have $V_A = 1$. It shows measurements throughout the time evolution of $\langle V_A \rangle$, and as the simulator line shows, ideally it would remain exactly equal to 1 throughout the time evolution. The mitigated measurements show how, for most time measurements, we are able to produce $\langle V_A \rangle = 1$ within error bars.

We further note that the circuit depths for the simulations of the $\mathbb{Z}_2$ theory on the square plaquette lead to circuit volumes clearly greater than the quantum volume V_Q measurements of the quantum hardware ($d = 8$, $m = 5$, leading to a circuit volume of 40 for the square plaquette; whereas V_Q is 16 on IBM Q Valencia, suggesting a maximum square circuit volume of 16, with $d = m = 4$). The simple mitigation techniques employed thus seem to allow us to “beat” the quantum volume limitations for the hardware and get results consistent with the simulator within errors. For the triangular plaquette on IBM Q Bogota, we have $d = 8$, $m = 4$, leading to a circuit volume of 32; whereas the V_Q of the hardware is 32, corresponding to a $d = m = 5$ square. It is less clear whether we have exceeded quantum volume limitations for this simulation, and indeed, empirically, most Loschmidt probability data seems to meet the IBM Q threshold of 67% of the ideal amplitude [78], but again, we see that our mitigation efforts are successful at restoring the full measurement values.

B. $U(1)$ Theory on single plaquettes

We next present the data for the $U(1)$ theory on a single square plaquette and a single triangular plaquette, which we ran on IBM Q Quito and IBM Q Manila, respectively. Similarly to the $\mathbb{Z}_2$ case, IBM Q Quito has a T-shaped architecture [as seen in Fig. 6(b)] with $V_Q = 16$, while IBM Q Manila has a linear topology [as seen in Fig. 6(a)] with

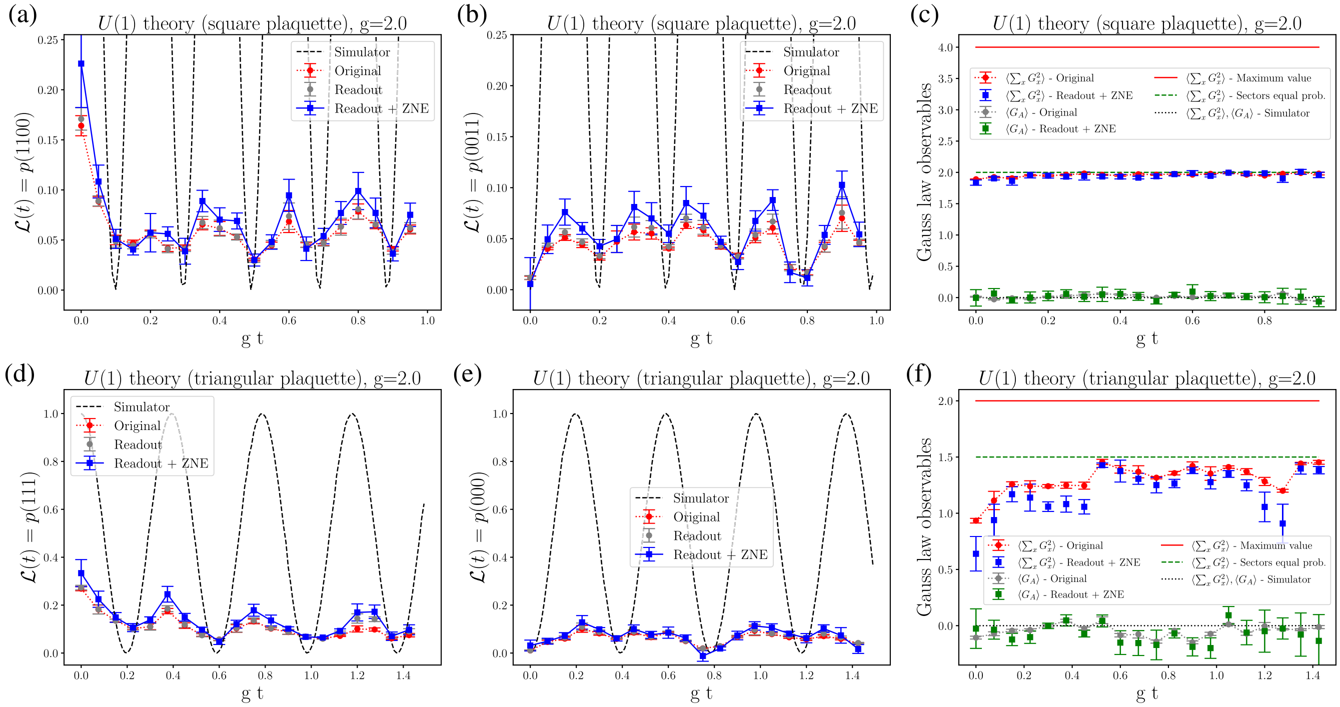

FIG. 11. Real-time evolution of the $U(1)$ theory on a single plaquette. The top row shows results for the square plaquette on IBM Q Quito hardware, with plots (a) and (b) showing Loschmidt probability data, and then plot (c) showing different Gauss law observables G_A and $\sum_x G_x^2$, with G_x defined as in Eq. (10). The bottom row shows results for the triangular plaquette on IBM Q Manila hardware, with again the first two plots (d) and (e) showing Loschmidt probability data, and plot (f) showing the G_A and $\sum_x G_x^2$ Gauss law observables.

$V_Q = 32$. We ran the square plaquette simulation on the T-shaped architecture because despite its lower V_Q, the topological advantages requiring fewer two-qubit gates made for better data. Indeed, we could not get any signal at all for the square plaquette $U(1)$ model on current linear-topology IBM Q devices.

Figure 11 shows the data for the $U(1)$ simulations. The first row of plots gives the square plaquette simulation data, with the first two plots, Figs. 11(a) and 11(b), showing Loschmidt probability data for the two states $|1100\rangle$ and $|0011\rangle$ in the $G_x = 0$ sector. Here we are running circuits that have much greater volume than the quantum volume limitations, with $m = 5$ and $d = 80$, and so we cannot come close to the correct amplitudes of the oscillations (shown by the dashed simulator lines), but we are able to make out some oscillations and see some qualitative similarity between the experimental data and the simulator data. It is clear, however, that the folding ZNE is unable to improve the accuracy of the data at this level.

The last plot in the top row, Fig. 11(c), is a test of how well the time-evolved system stays in the $G_x = 0$ sector by measuring two quantities: G_A in particular and then $\sum_x G_x^2$. For both of these quantities, we would expect to get zero in the ideal case, and indeed the data for G_A stays quite close to zero. As this is a simple average of G_A, however, we cannot rule out that many G_A measurements of $+1$ and -1 also exist in roughly equal quantities and are being averaged away, and indeed the leakage seen from the other plots suggests this must be occurring. We can quantify this leakage better by additionally measuring $\sum_x G_x^2$, which ideally should also be equal to 0 at all times. Here we also plot two lines: one at 4, which is the maximum value one could possibly get [by staying in the $G_x = \pm 1$ sectors, because the observable would be $4 \times (\pm 1)^2 = 4$], and one at 2, which is the value one would get if all sectors were equally represented in the time evolution [for the 16-sector average, we would get $(2 \times 0 + 12 \times 2 + 2 \times 4)/16 = 2$]. When we look at our experimental data, we see that indeed the measurements are quite close to all sectors being equally likely, but they are mostly slightly below that line. This suggests a slight bias toward the $G_x = 0$ sector.

The second row of Fig. 11 shows the data for the $U(1)$ theory on the triangular plaquette, with the first two plots, Figs. 11(d) and 11(e), giving the Loschmidt probability for states $|000\rangle$ and $|111\rangle$, which are the two states in the $G_x = 0$ sector. Again, with $d = 4$ and $m = 40$, we are likely far past the volume threshold suggested by $V_Q = 32$, and indeed the original data never comes close to the maximum amplitudes of 1 in the oscillations. However, again we are able to make out a qualitative agreement in behavior. We also see a close agreement in the frequency of

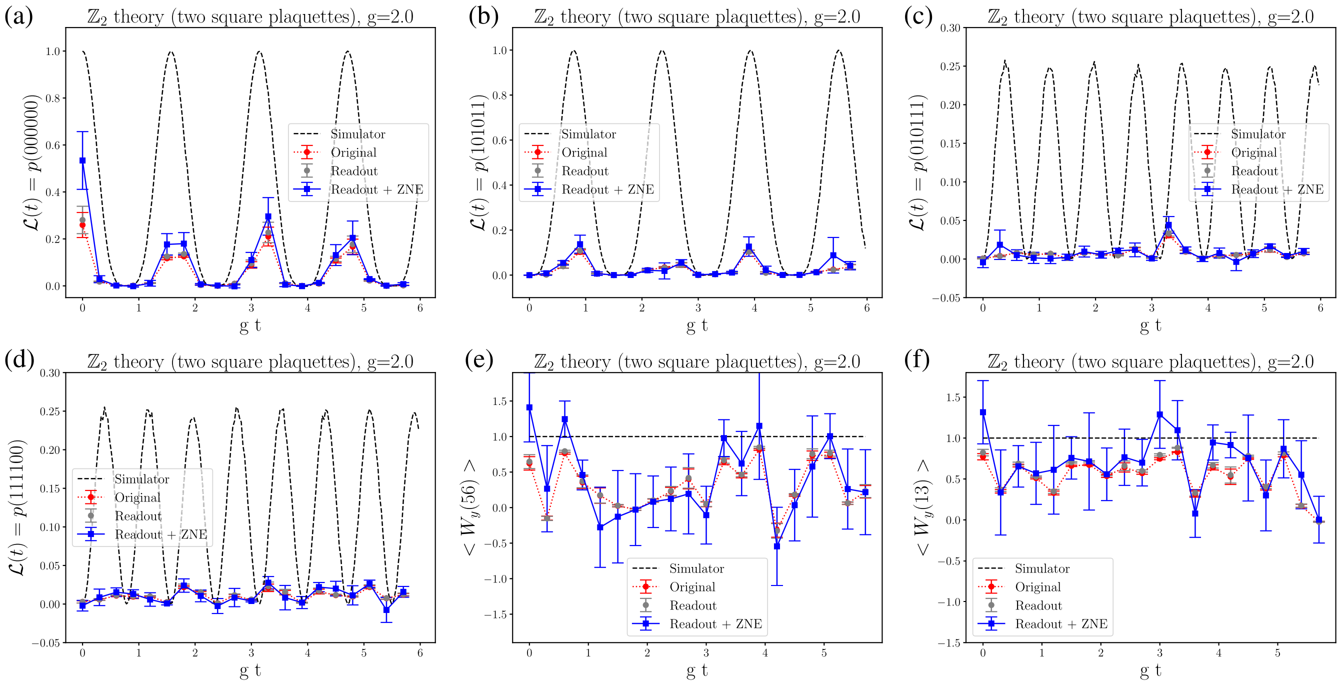

FIG. 12. Plots for the two-plaquette $\mathbb{Z}_2$ system, which was run on IBM Lagos. The first two plots (a) and (b) give the Loschmidt probabilities for states $|000000\rangle$ and $|101011\rangle$ which oscillate between 0 and 1, and the next two plots (c) and (d) give the Loschmidt probabilities for states $|010111\rangle$ and $|111100\rangle$, which oscillate between 0 and 0.25. The last two plots (e) and (f) are for the winding number observables in the y direction, the first involving links 5 and 6, and the second involving links 1 and 3, as defined in Fig. 4.

the oscillations, and that ZNE does still incrementally improve the results, unlike in the square plaquette case.

The last plot, Fig. 11(f) in the bottom row, again measures G_A and $\sum_x G_x^2$, and again the G_A observable is mostly close to 0, but once more, this can be explained by "leaky" states in both the $G_A = 1$ and $G_A = -1$ sectors also being sampled (so long as both the $G_A = 1$ and $G_A = -1$ errors are equally likely). We see this more clearly by measuring $\sum_x G_x^2$ as well. Again, we show two lines for comparison: the "maximum value" line shows the case where we get the largest value for the triangular plaquette, which occurs when $G_x = \pm 1$ for two of the sites and $G_x = 0$ for the third site. This results in an average value of 2, and we see that our experimental values are well below that. The second line again shows the value we would get if all sectors in the time evolution were equally likely [obtained by computing $(2 \times 0 + 6 \times 2)/8 = 3/2$ for the eight sectors of the triangular plaquette system]. Here we see quite clearly that even though our experimental data for $\sum_x G_x^2$ is much larger than 0, it is also clearly smaller than $3/2$, indicating a clear bias toward the $G_x = 0$ sector.

C. $\mathbb{Z}_2$ Theory: Two-plaquette system

Finally, we turn to the time evolution of the $\mathbb{Z}_2$ theory on the two-square-plaquette system, whose ideal behavior is shown in Fig. 5, where we see that if the system's initial state is in the sector where $G_x = 1$, the system's evolution involves only the four states that fall into that sector. As illustrated by Fig. 4, we are using periodic boundary conditions, and so there are six distinct links in the two-square-plaquette system. With the addition of an ancillary qubit, that brings us to seven qubits minimum for our simulation, and so we have used the seven-qubit IBM Lagos device to obtain real-time dynamics data.

Figure 12 gives the results for the simulation, with the first four plots, Figs. 12(a)–12(d), giving Loschmidt probability data for the four states in the $G_x = 1$ sector, which we label $|000000\rangle$, $|101011\rangle$, $|010111\rangle$, and $|111100\rangle$ in reference to the numbered links in Fig. 4. The $V_Q = 32$ for IBM Lagos tells us that the maximum square circuit meeting the accuracy threshold is 5×5. Comparing that to the two-plaquette-system circuit requirement with $m = 7$, $d = 48$ indicates that we are way beyond the quantum volume limit. However, especially for the states $|000000\rangle$ and $|101011\rangle$, where the simulator shows us the maximum amplitude goes up to 1, we are able to see qualitative agreement, and the readout error and ZNE error corrections do provide incremental improvements to the results.

The last two plots, Figs. 12(e) and 12(f), give data for the winding number observable W_y, defined in Eq. (20). As noted from before, the winding number in the y direction can be measured using links 1 and 3 as well as links 5 and 6, and in each case the result should be the same throughout the time evolution for the initial conditions that we chose: $W_y = 1$. Indeed, when we take the data and use ZNE, we do see a bias in the data closer to $+1$ than -1 for both W_y observables. As discussed in Sec. II, the winding number is a topological quantity, which is dependent on how the spins along a line spanning the entire system behaves. It is thus expected that this quantity could be robust against decoherence noise. In fact, our results here qualitatively confirm this, since we see that the winding number expectation value stays close to the winding number sector that the initial state belonged to. Of course, one needs to verify this on larger circuits.

VI. CONCLUSIONS

In this paper, we have explored the possibilities for real-time simulations of plaquette theories on current NISQ hardware, including theories with $\mathbb{Z}_2$ symmetries as well as the $U(1)$ symmetry, which is of particular interest from the QED perspective. We find that for the $\mathbb{Z}_2$ single-plaquette models, we can successfully overcome quantum volume, V_Q, limitations with the error mitigation schemes of readout error mitigation, as well as ZNE through circuit folding. In cases where the circuit significantly exceeds the quantum volume, such as the cases of the two-plaquette $\mathbb{Z}_Z$ model and the $U(1)$ models, the error mitigation does not have a significant effect on the results. However, since the error mitigation techniques used are hardware agnostic, this has promising implications for NISQ devices in general, rather than only on IBM Q devices. Even in cases where we cannot overcome V_Q limitations, we are still able to see qualitative signals of the real-time dynamics for circuits that are many times deeper than the V_Q measurements for the hardware. We have seen that topology is also an important consideration for quantum simulations with superconducting qubits in particular, and found significant quantitative advantages in choosing the best topology for each experiment.

Future improvements specific to superconducting qubits would involve using pulse control for ZNE rather than folding, as well as denser data points to capture the time evolution for a plaquette model. Additionally, future work could involve simulating the real-time dynamics of non-Abelian plaquette models. Another immediate attempt would be to use different encoding strategies already with the microscopic model. For example, the $U(1)$ or the $\mathbb{Z}_2$ models can be represented in terms of dual height variables in two spatial dimensions, which already removes much of the gauge noninvariant states. Formulating quantum circuits on the dualized versions of such models would enable bigger lattices to be realized on quantum circuits [70]. Similarly, the use of rishons allows a gauge-invariant formulation of several non-Abelian gauge theories such as the aforementioned $SO(3)$-symmetric model, which can then be used to construct quantum circuits on NISQ devices [63,83].

The source code for our experiments is available at [84].

ACKNOWLEDGMENTS

We would like to thank Sebastian Hassinger and Roger Melko for arranging an IBM Q Experience for Academic Research Program Agreement (No. W1975852) for us. We acknowledge the use of IBM Quantum services for this work. The views expressed are those of the authors, and do not reflect the official policy or position of IBM or the IBM Quantum team. We would also like to thank the Unitary Fund for additional research account access. Thanks are due to Lukas Rammelmüller for providing valuable suggestions on an earlier draft. Research by E. H. at the Perimeter Institute is supported in part by the Government of Canada through the Department of Innovation, Science and Economic Development and by the Province of Ontario through the Ministry of Colleges and Universities.

---

[1] F. Wilczek, Phys. Scr. **T168**, 014003 (2016).
[2] J. Preskill, Quantum **2**, 79 (2018).
[3] C. Noh and D. G. Angelakis, Rep. Prog. Phys. **80**, 016401 (2016).
[4] P. Krantz, M. Kjaergaard, F. Yan, T. P. Orlando, S. Gustavsson, and W. D. Oliver, Appl. Phys. Rev. **6**, 021318 (2019).
[5] B. P. Lanyon, C. Hempel, D. Nigg, M. Muller, R. Gerritsma, F. Zahringer, P. Schindler, J. T. Barreiro, M. Rambach, G. Kirchmair *et al.*, Science **334**, 57 (2011).
[6] I. Bloch, J. Dalibard, and S. Nascimbène, Nat. Phys. **8**, 267 (2012).
[7] R. P. Feynman, Int. J. Theor. Phys. **21**, 467 (1982).
[8] A. Parra-Rodriguez, P. Lougovski, L. Lamata, E. Solano, and M. Sanz, Phys. Rev. A **101** (2020).
[9] M. Srednicki, Phys. Rev. E **50**, 888 (1994).
[10] J. M. Deutsch, Phys. Rev. A **43**, 2046 (1991).
[11] F. Alet and N. Laflorencie, C.R. Phys. **19**, 498 (2018).
[12] J. Smith, A. Lee, P. Richerme, B. Neyenhuis, P. W. Hess, P. Hauke, M. Heyl, D. A. Huse, and C. Monroe, Nat. Phys. **12**, 907 (2016).
[13] M. Serbyn, D. A. Abanin, and Z. Papić, Nat. Phys. **17**, 675 (2021).
[14] M. C. Bañuls *et al.*, Eur. Phys. J. D **74**, 165 (2020).
[15] E. A. Martinez *et al.*, Nature (London) **534**, 516 (2016).

[16] H. Bernien, S. Schwartz, A. Keesling, H. Levine, A. Omran, H. Pichler, S. Choi, A. S. Zibrov, M. Endres, M. Greiner *et al.*, Nature (London) **551**, 579 (2017).

[17] C. Schweizer, F. Grusdt, M. Berngruber, L. Barbiero, E. Demler, N. Goldman, I. Bloch, and M. Aidelsburger, Nat. Phys. **15**, 1168 (2019).

[18] A. Mil, T. V. Zache, A. Hegde, A. Xia, R. P. Bhatt, M. K. Oberthaler, P. Hauke, J. Berges, and F. Jendrzejewski, Science **367**, 1128 (2020).

[19] B. Yang, H. Sun, R. Ott, H.-Y. Wang, T. V. Zache, J. C. Halimeh, Z.-S. Yuan, P. Hauke, and J.-W. Pan, Nature (London) **587**, 392 (2020).

[20] Z. Davoudi, M. Hafezi, C. Monroe, G. Pagano, A. Seif, and A. Shaw, Phys. Rev. Res. **2**, 023015 (2020).

[21] H. Lamm and S. Lawrence, Phys. Rev. Lett. **121**, 170501 (2018).

[22] E. Gustafson, Y. Meurice, and J. Unmuth-Yockey, Phys. Rev. D **99**, 094503 (2019).

[23] E. Gustafson, P. Dreher, Z. Hang, and Y. Meurice, Quantum Sci. Technol. **6**, 045020 (2021).

[24] N. Klco, E. F. Dumitrescu, A. J. McCaskey, T. D. Morris, R. C. Pooser, M. Sanz, E. Solano, P. Lougovski, and M. J. Savage, Phys. Rev. A **98**, 032331 (2018).

[25] N. Klco, M. J. Savage, and J. R. Stryker, Phys. Rev. D **101**, 074512 (2020).

[26] J. Zhang, J. Unmuth-Yockey, J. Zeiher, A. Bazavov, S.-W. Tsai, and Y. Meurice, Phys. Rev. Lett. **121**, 223201 (2018).

[27] R. Lewis and R. M. Woloshyn, arXiv:1905.09789.

[28] Y. Atas, J. Zhang, R. Lewis, A. Jahanpour, J. F. Haase, and C. A. Muschik, Nat. Commun. **12**, 6499 (2021).

[29] J. R. Stryker, Phys. Rev. A **99**, 042301 (2019).

[30] I. Raychowdhury and J. R. Stryker, Phys. Rev. D **101**, 114502 (2020).

[31] I. Raychowdhury and J. R. Stryker, Phys. Rev. Res. **2**, 033039 (2020).

[32] Z. Davoudi, I. Raychowdhury, and A. Shaw, Phys. Rev. D **104**, 074505 (2021).

[33] N. Klco and M. J. Savage, Phys. Rev. A **99**, 052335 (2019).

[34] N. Klco and M. J. Savage, Phys. Rev. A **102**, 052422 (2020).

[35] A. Ciavarella, N. Klco, and M. J. Savage, Phys. Rev. D **103**, 094501 (2021).

[36] J. Bender and E. Zohar, Phys. Rev. D **102**, 114517 (2020).

[37] M. Aidelsburger, L. Barbiero, A. Bermudez, T. Chanda, A. Dauphin, D. González-Cuadra, P. R. Grzybowski, S. Hands, F. Jendrzejewski, J. Jünemann *et al.*, Phil. Trans. R. Soc. A **380**, 20210064 (2021).

[38] E. Zohar, Phil. Trans. R. Soc. A **380**, 20210069 (2021).

[39] V. Kasper, D. González-Cuadra, A. Hegde, A. Xia, A. Dauphin, F. Huber, E. Tiemann, M. Lewenstein, F. Jendrzejewski, and P. Hauke, Quantum Sci. Technol. **7**, 015008 (2022).

[40] L. Funcke, T. Hartung, K. Jansen, S. Kühn, and P. Stornati, Quantum **5**, 422 (2021).

[41] P. W. Shor, Phys. Rev. A **52**, R2493 (1995).

[42] A. M. Steane, Phys. Rev. Lett. **77**, 793 (1996).

[43] Y. Li and S. C. Benjamin, Phys. Rev. X **7**, 021050 (2017).

[44] A. Kandala, K. Temme, A. D. Córcoles, A. Mezzacapo, J. M. Chow, and J. M. Gambetta, Nature (London) **567**, 491 (2019).

[45] A. He, B. Nachman, W. A. de Jong, and C. W. Bauer, Phys. Rev. A **102**, 012426 (2020).

[46] R. LaRose *et al.*, Quantum **6**, 774 (2022).

[47] T. Giurgica-Tiron, Y. Hindy, R. LaRose, A. Mari, and W. J. Zeng, *2020 IEEE International Conference on Quantum Computing and Engineering (QCE)* (IEEE, Denver, CO, USA, 2020), 10.1109/QCE49297.2020.00045.

[48] A. Lowe, M. H. Gordon, P. Czarnik, A. Arrasmith, P. J. Coles, and L. Cincio, Phys. Rev. Res. **3**, 033098 (2021).

[49] A. Sopena, M. H. Gordon, G. Sierra, and E. López, Quantum Sci. Technol. **6**, 045003 (2021).

[50] S. McArdle, X. Yuan, and S. Benjamin, Phys. Rev. Lett. **122**, 180501 (2019).

[51] L. Funcke, T. Hartung, K. Jansen, S. Kühn, P. Stornati, and X. Wang, Phys. Rev. A **105**, 062404 (2022).

[52] B. Nachman, M. Urbanek, W. A. de Jong, and C. W. Bauer, npj Quantum Inf. **6**, 84 (2020).

[53] M. S. Jattana, F. Jin, H. De Raedt, and K. Michielsen, Quantum Inf. Process. **19**, 414 (2020).

[54] N. Klco and M. J. Savage, Phys. Rev. A **104**, 062425 (2021).

[55] D. Horn, Phys. Lett. **100B**, 149 (1981).

[56] P. Orland and D. Rohrlich, Nucl. Phys. **B338**, 647 (1990).

[57] S. Chandrasekharan and U. J. Wiese, Nucl. Phys. **B492**, 455 (1997).

[58] See Supplemental Material at http://link.aps.org/supplemental/10.1103/PhysRevD.106.094502 for details into the circuit identity proofs and exact solutions used, as well as resource scaling calculations and information regarding the fluctuations of the IBM Q device measurements.

[59] M. Carena, H. Lamm, Y.-Y. Li, and W. Liu, Phys. Rev. Lett. **129**, 051601 (2022).

[60] E. J. Gustafson, Phys. Rev. D **103**, 114505 (2021).

[61] J. Kogut and L. Susskind, Phys. Rev. D **11**, 395 (1975).

[62] K. Symanzik, Nucl. Phys. **B226**, 187 (1983).

[63] E. Rico, M. Dalmonte, P. Zoller, D. Banerjee, M. Bögli, P. Stebler, and U.-J. Wiese, Ann. Phys. (Amsterdam) **393**, 466 (2018).

[64] M. Müller, K. Hammerer, Y. L. Zhou, C. F. Roos, and P. Zoller, New J. Phys. **13**, 085007 (2011).

[65] A. Mezzacapo, E. Rico, C. Sabín, I. L. Egusquiza, L. Lamata, and E. Solano, Phys. Rev. Lett. **115**, 240502 (2015).

[66] A. Kitaev, Ann. Phys. (Amsterdam) **303**, 2 (2003).

[67] N. Shannon, G. Misguich, and K. Penc, Phys. Rev. B **69**, 220403 (2004).

[68] M. Hermele, M. P. A. Fisher, and L. Balents, Phys. Rev. B **69**, 064404 (2004).

[69] R. C. Brower, D. Berenstein, and H. Kawai, Proc. Sci., LATTICE2019 (**2020**) 112 [arXiv:2002.10028], https://pos.sissa.it/363/112/pdf.

[70] D. Banerjee, S. Caspar, F. J. Jiang, J. H. Peng, and U. J. Wiese, arXiv:2107.01283.

[71] M. Heyl, Europhys. Lett. **125**, 26001 (2019).

[72] D. Banerjee, F.-J. Jiang, P. Widmer, and U.-J. Wiese, J. Stat. Mech. (2013) P12010.

[73] D. Banerjee and A. Sen, Phys. Rev. Lett. **126**, 220601 (2021).

[74] D. Marcos, P. Widmer, E. Rico, M. Hafezi, P. Rabl, U. J. Wiese, and P. Zoller, Ann. Phys. (Amsterdam) **351**, 634 (2014).

[75] A. W. Glaetzle, M. Dalmonte, R. Nath, C. Gross, I. Bloch, and P. Zoller, Phys. Rev. Lett. **114**, 173002 (2015).
[76] A. Celi, B. Vermersch, O. Viyuela, H. Pichler, M. D. Lukin, and P. Zoller, Phys. Rev. X **10**, 021057 (2020).
[77] N. M. Linke, D. Maslov, M. Roetteler, S. Debnath, C. Figgatt, K. A. Landsman, K. Wright, and C. Monroe, Proc. Natl. Acad. Sci. U.S.A. **114**, 3305 (2017).
[78] A. W. Cross, L. S. Bishop, S. Sheldon, P. D. Nation, and J. M. Gambetta, Phys. Rev. A **100**, 032328 (2019).
[79] Z. Chen *et al.*, Nature (London) **595**, 383 (2021).
[80] M. R. Geller, Quantum Sci. Technol. **5**, 03LT01 (2020).
[81] F. B. Maciejewski, Z. Zimborás, and M. Oszmaniec, Quantum **4**, 257 (2020).
[82] M. S. Anis *et al.*, QISKIT: An open-source framework for quantum computing (2021), 10.5281/zenodo.2573505.
[83] R. Brower, S. Chandrasekharan, and U.-J. Wiese, Phys. Rev. D **60**, 094502 (1999).
[84] E. Huffman, M. García Vera, and D. Banerjee, Plaquette-models, 2022, 10.5281/zenodo.7150653.